

Permeability of water through a raft model membrane clarified by time-resolved SANS and SAXS

Mitsuhiro Hirai,^{a*} Teruaki Onai,^a Masaharu Koizumi,^a Harutaka Hirai,^a Kohji Kasahara,^b Naoko Suzuki,^b Kohei Yuyama^b and Katsuaki Inoue^c

^aDepartment of Physics, Gunma University, Maebashi 371-8510, Japan, ^bThe Tokyo Metropolitan Institute of Medical Science, Tokyo 113-8613, Japan, and ^cJapan Synchrotron Radiation Research Institute, Sayo Hyogo 679-5198, Japan. Correspondence e-mail: mhirai@fs.aramaki.gunma-u.ac.jp

We have characterized the structures of ganglioside (G_{D3}) micelle and G_{D3} /cholesterol mixtures, and have determined the permeability of water across a membrane of G_{D3} /cholesterol/phospholipid uni-lamellar vesicle. We have found that monovalent Na^+ and K^+ cations affect the permeability of water differently. We have found also that the permeability of water is greatly enhanced by the K^+ ion, suggesting the function of the G_{D3} /cholesterol rich clusters on neuronal excitations by K^+ . The complimentary use of small-angle X-ray and neutron scattering techniques is useful to determine the permeability of water across a vesicle membrane.

© 2007 International Union of Crystallography
 Printed in Great Britain – all rights reserved

1. Introduction

To clarify the permeability of water through lipid bilayers, we have carried out the time-resolved measurements of small unilamellar vesicle (SUV) of ternary lipid mixtures using small-angle neutron scattering (SANS) and small-angle X-ray scattering (SAXS). The lipid mixtures we have studied are composed of glycosphingolipid (GSL)/cholesterol/phospholipid, which is regarded as a model plasma membrane containing so-called rafts. The rafts are lipid microdomains in mammalian plasma membrane, which are assumed to play important roles in various events on plasma membranes such as signal transduction, cell adhesion and lipid/protein sorting (Simons & Ikonen, 1997; Simons *et al.*, 1998; Simons & Toomre, 2000). A common feature of plasma membrane microdomains is their peculiar lipid composition, being rich in glycosphingolipids (GSLs), sphingomyelin and cholesterol. Gangliosides, major components of GSLs, are acidic lipids composed of a ceramide linked to an oligosaccharide chain containing one or more sialic acid residues. In spite of numerous results accumulated on the physiological functions of GSLs and those microdomains (Ledeen *et al.*, 1998; Hakomori, 2001; Kasahara & Sanai, 2001; Yuyama *et al.*, 2003), how GSL microdomains function in membranes and how they modulate membrane properties have remained ambiguous (Heerklotz, 2002). By using SANS, SAXS and neutron spin echo (NSE) techniques we clarified several notable characteristics of the structures and dynamics of ganglioside micelles and ganglioside-containing vesicles, depending on temperature, pH, salt concentrations and lipid compositions. We have found the following characteristics. (1) Gangliosides (monosialoganglioside G_{M1} , G_{M3} ; disialogangliosides G_{D1a} , G_{D1b} ; trisialoganglioside G_{T1b}) form an ellipsoidal micelle whose sugar-chain regions are a very hydrophilic. With increases in temperature, hydration and dehydration of sugar chains occur with the conformational change of bending (Hirai *et al.*, 1996*a,b*, 1998*a,b*; Hayakawa & Hirai, 2002) and change in the degree of dissociation of sialic acids (Hirai *et al.*, 1996*c*, 1999). These changes accompany thermal hysteresis depending on the sugar head (Hayakawa & Hirai, 2002).

(2) In ganglioside (G_{M1})/phospholipid (DPPC, dipalmitoyl phosphocholine) mixed SUV system gangliosides predominantly locate at the outer-leaflet of the vesicle as occurs in plasma membranes (Hirai *et al.*, 2003). (3) In the cases of ganglioside (G_{M1} , G_{D1a} , G_{D1b} , G_{T1b})-cholesterol binary systems we found the presence of maximum miscibility of cholesterol within gangliosides, cholesterol-dependent micelle-to-vesicle transitions (G_{M1}), and Ca-induced vesicle-to-lamellar transitions (G_{M1}) accompanying the formation of an interdigitated structure between the sugar heads in the opposing bilayers (Hayakawa & Hirai, 2003; Hirai *et al.*, 2005). (4) From the NSE experiments, the dehydration and the bending of sugar heads suppress the undulation of the ganglioside micellar structure (Hirai *et al.*, 2001). In the case of ganglioside-cholesterol-phospholipid (DSPC, distearoyl phosphocholine; DOPC, dioleoyl phosphocholine; POPC, palmitoyl-oleoyl phosphocholine; PC, L- α -phosphocholine) ternary SUV systems, the bending modulus tends to take the smallest value at the lipid composition of ganglioside/cholesterol/glycerophospholipid $\approx 0.1/0.1/1$. This is similar to intact neuronal cells including rafts, meaning that the ganglioside-cholesterol microdomains can afford an appropriate fluidity to membranes and to hold a homeostasis of membrane environments. Our previous results suggest that the microdomains enriched in ganglioside and cholesterol can not only locally modulate charge and hydrophilicity of plasma membrane surfaces but also dominate the dynamics of plasma membranes, which are essentially important for transmembrane signaling such as the accumulation and activation of functional proteins.

In the present report we treat the structural properties of disialoganglioside (G_{D3}) micelle, G_{D3} /cholesterol and G_{D3} /cholesterol/PC mixtures. One of the authors showed that G_{D3} is associated with Src family tyrosine kinase (Lyn) and with the glycosylphosphatidylinositol-anchored signaling protein (TAG-1), in glycosphingolipid-enriched microdomains in rat brain and that G_{D3} regulates Lyn in a caveolae-like domain on brain cell membranes (Kasahara *et al.*, 1997, 2000). On the other hand, G_{D3} synthase knockout mice expressing only monosialoganglioside G_{M3} as their major ganglioside exhibit lethal audiogenic seizures (Kawai *et al.*,

2001). In addition KCl-treatment of PC12 cells was shown to induce depolarization of the plasma membrane and Ca²⁺ influx into the cells and to activate Lyn on stimulation with KCl (Kasahara *et al.*, 1998). These results suggest that KCl might induce intracellular signaling with nerve excitation mediated by the interaction with G_{D3}. Thus, the physicochemical properties of G_{D3} and G_{D3} containing lipid mixtures, especially the response of those aggregates to KCl are expected to give an insight to the biological functions of G_{D3}.

2. Materials and methods

2.1. Sample preparation

Disialogangliosides (G_{D13}, II³NeuAc₂-Lac-Cer) from bovine milk purchased from WAKO Chemical Co. (USA), and cholesterol purchased from SIGMA Chemical Co. (USA) and PC (1- α -phosphocholine) from Avanti Polar Lipids Inc. were used without further purification. All other chemicals used were of analytical grade. For the preparation of G_{D3}/cholesterol and G_{D3}/cholesterol/PC mixed samples, required quantities of G_{D3}, cholesterol and PC for each sample were dissolved in a 2:1 (v/v) mixture of chloroform and methanol. After removing the organic solvent in a stream of nitrogen gas, the lipid mixtures were dried at 318 K *in vacuo* overnight. The dried mixtures were suspended in H₂O solvent with 50 mM HEPES [N-(2-hydroxymethyl)piperazine-N'-(2-ethanesulfonic acid)] buffer adjusted to pH 7.0 to become 1.0 or 0.5 wt% lipid concentration, and the mixture was stirred for several minutes. For the preparation of the SUV, samples of the above mixtures were sonicated for 10 min using a high-power probe-type ultrasonicator (Model UH-50 of SMT Co.) at 50 W. In the permeability experiments, the lipid mixture of 5% w/v in H₂O HEPES buffer was mixed with the D₂O HEPES at pH 7 containing sodium or potassium salt in a 1/4 volume ratio. The final lipid and salt concentrations were 1% w/v and 50 mM, respectively. Just after the mixing (dead time ~5 min), the measurements were started.

2.2. Neutron and X-ray scattering measurements

SANS measurements were carried out by using a spectrometer installed at C1-2 beam port of the research reactor JRR-3M of Japan Atomic Energy Agency (JAER), Tokai, Japan. The neutron wavelength used was 7.0 Å. The sample to two-dimensional area detector distance was 4 m. The exposure time was 30 min. SAXS measurements were carried out using a spectrometer installed at the BL-15A beam port of the synchrotron radiation source (PF) at the High Energy Accelerator Research Organization (KEK), Tsukuba, Japan (Ueki *et al.*, 1985). The X-ray wavelength, the sample-to-detector

distance and the exposure time were 1.49 Å, 80 cm and 300 s, respectively. The scattering intensity was detected by a one-dimensional position sensitive proportional counter. Wide-angle X-ray scattering (WAXS) measurements were carried out using a spectrometer installed at BL-40 of 8 GeV synchrotron radiation source at the Japan Synchrotron Radiation Research Institute (JASRI), Harima, Japan (Miura *et al.*, 2000). The X-ray wavelength and the sample-to-detector distance were 0.729 Å and 46 cm, respectively. X-ray scattering intensity was detected by a Rigaku R-Axis IV imaging plate system (IP 30 × 30 cm² in area). Details of the background correction for the WAXS data have been described elsewhere (Hirai *et al.*, 2002, 2004). In the SANS, SAXS and WAXS measurements, the temperatures of the samples were controlled at 298 K.

2.3. Scattering data treatments and modeling

The following standard analyses of X-ray and neutron scattering data were carried out as reported previously (Hirai *et al.*, 1996a, 2003). The distance distribution function $p(r)$ was obtained by Fourier transform of the observed scattering intensity $I(q)$ as

$$p(r) = \frac{1}{2\pi^2} \int_0^\infty rql(q) \sin(rq) dq \quad (1)$$

where $q = (4\pi/\lambda) \sin(\theta/2)$, and q and λ are the scattering angle and the X-ray wavelength. The radius of gyration R_g was determined by

$$R_g^2 = \frac{\int_0^{D_{\max}} p(r)r^2 dr}{2 \int_0^{D_{\max}} p(r) dr} \quad (2)$$

where D_{\max} , the maximum diameter of the particle, was estimated from the function $p(r)$ satisfying the condition $p(r) = 0$ for $r > D_{\max}$. In the present model-fitting analysis, we used the spherical averaged scattering function $I(q, R)$ of an ellipsoidal particle with radius R composed of n shells with different average scattering densities given by

$$I(q, R) = \int_0^1 \left[3\{\rho_1 V_1 j_1(q, R_1)/(q, R_1)\} + \sum_{i=2}^n (\rho_i - \rho_{i-1}) V_i j_1(q, R_i)/(q, R_i) \right] dx \quad (3)$$

where ρ_i is the average excess scattering density (so-called contrast) of i th shell with a shape of an ellipsoid of rotation, j_1 is the spherical Bessel function of the first rank. R_i is defined as

$$R_i = r_i \{1 + x^2(v_i^2 - 1)\}^{1/2} \quad (4)$$

where r_i and v_i are the semiaxis and its ratio of i th ellipsoidal shell, respectively. The details of the shell modeling method have been given elsewhere (Hirai *et al.*, 1996a,b, 1998b, 1999).

3. Results and discussion

3.1. Characterization of G_{D3} micelle by WAXS

Fig. 1 shows the WAXS curve of G_{D3} micelle in 50 mM HEPES buffer at 298 K. As shown in Fig. 1, the WAXS curve measured covers the q -range from ~0.03 to ~2 Å⁻¹, namely the real space distance from ~210 to ~2 Å. The broad peak around 1.47 Å⁻¹ indicates the disordered packing of the hydrocarbon chains in the ceramide portions of G_{D3} molecules. The scattering curve below ~0.5 Å⁻¹ shows a strong ripple profile, which results from the form factor of the G_{D3} micelle. By using the model scattering function of equation (3), we are able to describe the experimental data at low region in Fig. 1. Figs. 2A and 2B show both the experimental and theoretical scat-

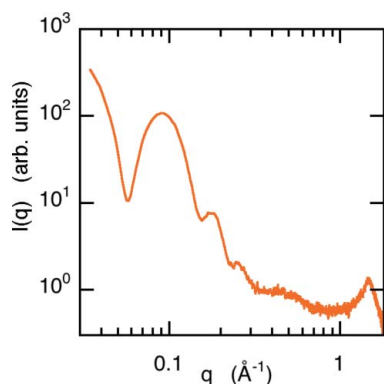


Figure 1 WAXS curve of G_{D3} micelle, 0.5%w/v in 50 mM HEPES buffer at pH 7, at 298 K.

tering curves and $p(r)$ functions, respectively. Here we applied the model scattering function of an ellipsoid composed of four shells to fit the experimental data in the q region of $0.035\text{--}0.4\text{ \AA}^{-1}$. The model fitting was carried out in two steps. In the first step we used a double-shelled ellipsoid structure composed of a hydrophilic shell (sugar head region) and a hydrophobic core (tail region) under the vicinity that comes from the maximum diameter given by Fig. 2B and from the extended lengths of head and tail regions. After the first-step optimization, as the second step each region was separated into two other regions, namely, a four-shelled model was used to execute further fitting of the experimental scattering curve. In spite of such a simple model, both the theoretical scattering curve and the final $p(r)$ function agree well with the experimental ones. The reliability factor R for the model scattering function defined by $R = \sum |I_{\text{exp}}(q) - I_{\text{model}}(q)| / \sum I_{\text{exp}}(q)$ is 0.026. The structural parameters determined for the optimized model are as follows. The radii, the axial ratios and the relative contrasts of the shells are $55\text{ \AA}/44\text{ \AA}/35\text{ \AA}/30\text{ \AA}$, $1.37/1.43/1.81/1.8$, and $0.31/0.58/1.43/0.60$ for the outer shell, respectively. The first and second shells mostly correspond to the hydrophilic oligosaccharide chain region including a hydration shell. The third and fourth shells correspond to the head and tail portion of the ceramide regions, respectively. The above parameters suggest that the G_{D3} micelle is surrounded by a hydrophilic region with a width of $\sim 20\text{ \AA}$. The G_{D3} molecule is composed of disaccharide combined with two sialic acid residues. In spite of the decrease in the number of sugar groups, the width ($\sim 20\text{ \AA}$) is mostly comparable with those of G_{D1a} and G_{M1} (Hirai *et al.*, 1996*a,b*, 1998*b*), indicating that the head portion of the G_{D1a} molecule takes an extended conformation due to an electrostatic and hydration repulsion between the polar heads. The third region with a high positive contrast would suggest the presence of a high electron density region, which might result from some

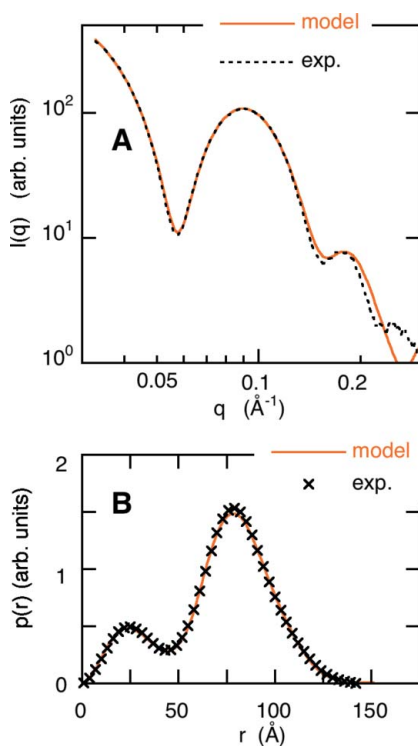


Figure 2
Experimental and theoretical WAXS scattering curves (A) and distance distribution $p(r)$ functions (B), respectively. Dotted lines and crosses correspond to experimental data. Experimental WAXS curve is as in Fig. 1.

interdigitated or zigzag packing of the G_{D3} molecules in the micellar form.

3.2. Structural changes to the G_{D3} -cholesterol mixture depending on the molar ratio observed by SAXS

Fig. 3 shows the cholesterol content dependence of the scattering curve of the mixture, where the molar ratio of $[G_{D3}]/[\text{cholesterol}]$ was varied from 1/0 to 1/3. On increasing the cholesterol content from 1/0 to 1/0.75 the scattering curve below 0.05 \AA^{-1} changes from a saturating profile to a steep slope, indicating the micelle to vesicle transition. Above 1/2 a kink or a broad peak around 0.08 \AA^{-1} appears, suggesting the coexistence of lamellar and vesicle phases.

The repeat distance of the lamellar phase is around 79 \AA . The $p(r)$ function in Fig. 4A evidently reflects the above changes. As shown in Fig. 4B, the radius of gyration tends to saturate with increasing cholesterol content, which is attributable to the presence of the maximum miscibility of cholesterol against G_{D3} , similar to the cases of other gangliosides (Hayakawa & Hirai, 2003; Hirai *et al.*, 2005). The increase above $[\text{cholesterol}]/[G_{D3}] = 2/1$ is ascribed to the appearance of the lamellar phase. The maximum miscibility of cholesterol is $\sim 1\text{--}2$ for G_{D3} .

3.3. Effect of monovalent salts on G_{D3} micelle and G_{D3} -cholesterol mixture revealed by SAXS

Figs. 5A and 5B show the monovalent salts (KCl and NaCl) concentration dependence of R_g of G_{D3} micelle and $[G_{D3}]/[\text{cholesterol}] = 1/0.5$ and $1/1$ SUVs, respectively, where the salt concentration was varied from 0 to 200 mM. In the case of the G_{D3} micelle shown in Fig. 5A, both salts induce a slight decrease of R_g from 57.6 ± 0.4 to $53.9 \pm 0.5\text{ \AA}$ for NaCl and from 57.6 ± 0.4 to $54.9 \pm 0.4\text{ \AA}$ for KCl. In the cases of the SUV of $[G_{D3}]/[\text{cholesterol}] = 1/0.5$, with increasing salt concentration the R_g vary from 94.7 ± 1.5 to $96.5 \pm 3.9\text{ \AA}$ for NaCl and from 94.7 ± 1.5 to $98.4 \pm 2.1\text{ \AA}$ for KCl, respectively. In the cases of the SUV of $[G_{D3}]/[\text{cholesterol}] = 1/1$, the values vary from 96.5 ± 1.3 to $98.1 \pm 5.0\text{ \AA}$ for NaCl and from 96.5 ± 1.3 to $77.7 \pm 5.1\text{ \AA}$ for KCl, respectively. Thus, except in the case of 1/1 SUV added with KCl salt, the values of R_g are mostly stable within experimental error. In other words, for the SUV around the maximum miscibility of cholesterol against G_{D3} , the KCl salt has the effect of changing the SUV structure.

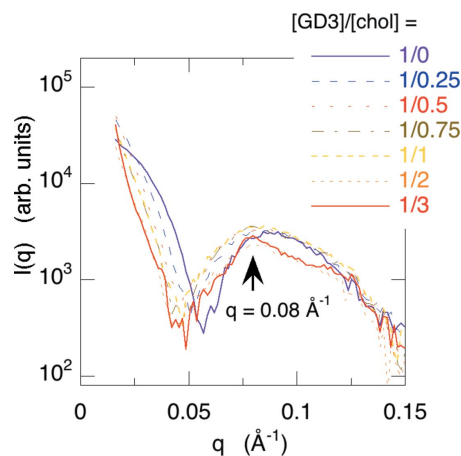


Figure 3
Variation of the SAXS curve of a G_{D3} -cholesterol binary mixture depending on cholesterol content (0.5% w/v total lipid, at pH 7, at 298 K). The molar ratio of $[G_{D3}]/[\text{cholesterol}]$ was varied from 1/0 to 1/3.

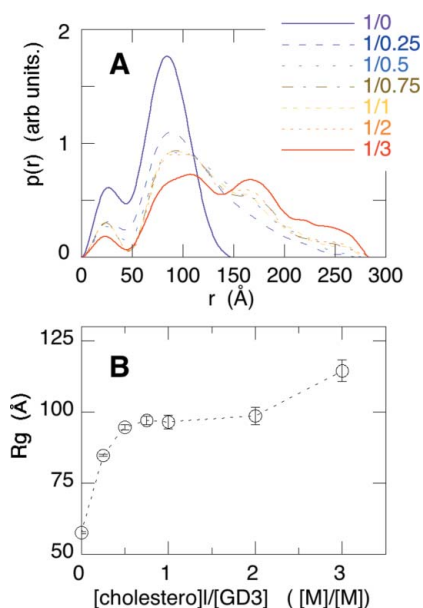


Figure 4
Cholesterol dependence of distance distribution function $p(r)$ and radius of gyration R_g of G_{D3} -cholesterol binary mixtures. Data used for $p(r)$ and R_g calculations are as in Fig. 3.

3.4. Time-resolved SANS of G_{D3} -cholesterol-PC mixed SUV after jumping salt concentration

Figs. 6A and 6B show the time course of the SANS curves of the SUV of $[G_{D3}]/[\text{cholesterol}]/[\text{PC}] = 0.1/0.1/1$ after increasing the concentrations of KCl and NaCl from 0 mM to 50 mM, respectively. It is clear that the jump of KCl concentration induces a change of the SANS curve, whereas the NaCl salt does not alter the SANS curve for half a day. Fig. 7 shows the time-dependence of R_g of the SUV for KCl and NaCl cases obtained from the SANS curves in Figs. 6A and 6B, respectively. The R_g value changes from 99 ± 3 to 122 ± 5 Å at 50 mM KCl. On the other hand the R_g of the SUV at 50 mM NaCl changes

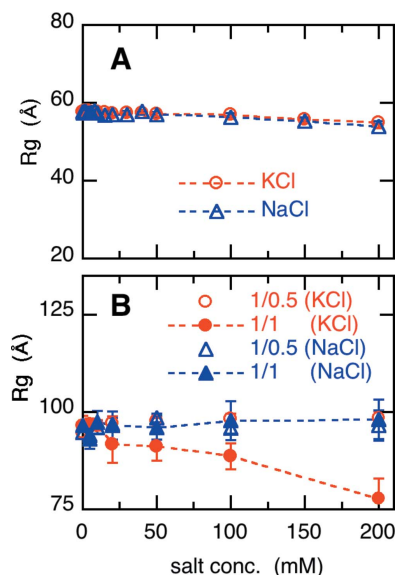


Figure 5
Monovalent salts (KCl and NaCl) concentration dependence of R_g of G_{D3} micelle (A) and $[G_{D3}]/[\text{cholesterol}] = 1/0.5$ and $1/1$ SUVs (B), respectively, where the salt concentration was varied from 0 to 200 mM.

from 95 ± 3 to 96 ± 2 Å, which is mostly stable for the whole period. Fig. 8 shows the SAXS curves of the SUV of $[G_{D3}]/[\text{cholesterol}]/[\text{PC}] = 0.1/0.1/1$, as same as used for the SANS, after the elevation of KCl salt concentration from 0 mM to 50 mM. We can recognize that there is little difference between the SAXS curves at initial and final times, indicating that the form factor of the SUV against X-ray is not altered for half a day. It should be mentioned that the SAXS measurement is unable to distinguish between the H_2O and D_2O water pools within the SUVs. In the present case the water pool SUV initially contains only H_2O . Thus, combined with the SANS and SAXS results shown in Figs. 6, 7 and 8, the change observed in the SANS curve at 50 mM KCl strongly suggests that the exchange of H_2O within the SUV water pool for D_2O in the solvent occurs through the bilayer. The increase of R_g would be reasonably explained as the change contrast profile of the SUV particle caused by this exchange as follows. At first we should consider the flux of the permeability of water molecules across the vesicle membrane. According to the general formulation, the flux of H_2O (J_H) and D_2O (J_D) are

$$J_H = P_H S (F_{SH} - F_{CH}) C = V_C C \frac{dF_{CH}}{dt}$$

$$J_D = P_D S (F_{SD} - F_{CD}) C = V_C C \frac{dF_{CD}}{dt} \quad (5)$$

where P_H and P_D are the permeability values of H_2O and D_2O at time t , F_{CH} , F_{CD} , F_{SH} and F_{SD} are the molar fractions of H_2O and D_2O in the water pool of the vesicle and in the solvent, C , V_C and S are the molar concentration of water, the volume of the water pool, the surface area of the vesicle, respectively. Due to the initial experi-

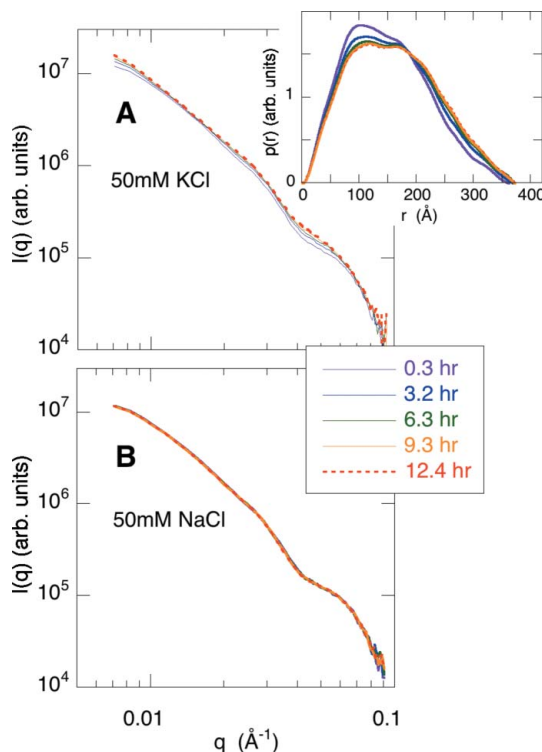
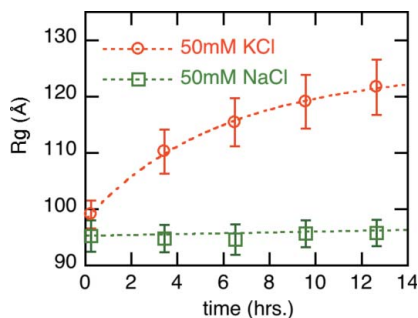


Figure 6
Time course of the SANS curves of the SUVs of $[G_{D3}]/[\text{cholesterol}]/[\text{PC}] = 0.1/0.1/1$ ternary mixtures after increasing the KCl and NaCl concentrations from 0 mM to 50 mM. The lipid concentrations were 1% w/v in 80% D_2O in 50 mM Hepes at pH 7. The water pool of SUV initially contained H_2O for both KCl and NaCl cases. Time-resolved SANS measurements were done for ~12 h at 298 K. The insert shows the time-dependence of $p(r)$ function of the SUV at 50 mM KCl.


Figure 7

Time-dependence of R_g of the SUVs of $[G_{D3}]/[\text{cholesterol}]/[\text{PC}] = 0.1/0.1/1$ after jumping the KCl and NaCl concentrations from 0 mM to 50 mM. These values were obtained from Fig. 6. The dotted lines show the least-squares fits as given in the text.

mental conditions ($F_{CH} = 1$ and $F_{CD} = 0$ at $t = 0$), F_{CH} and F_{CD} are solved as

$$\begin{aligned} F_{CH} &= (1 - F_{SH}) \exp(-P_H St/V_C) + F_{SH} \\ F_{CD} &= -F_{SD} \exp(-P_D St/V_C) + F_{SD} \end{aligned} \quad (6)$$

where F_{SH} and F_{SD} remain constant at 0.2 and 0.8 throughout the measurement because the volume of the vesicle was small compared with the volume outside. On the other hand the average excess scattering density ρ_e , so-called contrast, of the SUV at time t is given as

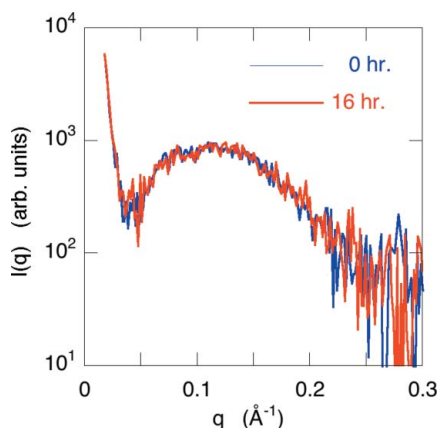
$$\rho_t = (\rho_C V_C + \rho_B V)/(V_C + V_B) - \rho_S \quad (7)$$

where V_B and ρ_B are the volume and average scattering density of the bilayer of the membrane, and ρ_S is the average scattering density of the solvent. By applying equation (6) to equation (7), we can obtain

$$\begin{aligned} \rho_t &= \left\{ (\rho_{H_2O} - \rho_{D_2O}) F_{SD} V_C \exp(-P_D St/V_C) + (\rho_B - \rho_S) V_L \right\} / (V_C + V_B) \\ &\equiv A \exp(-P_D St/V_C) + B \end{aligned} \quad (8)$$

where we place $P_H \approx P_D = P$, and A and B are negative values in the present case. Thus the contrast depends on the single exponential.

Based on the result from Fig. 8 that the shape of the SUV holds in the whole period and on the general definition of radius of gyration of a particle with a center symmetric scattering density distribution (Stuhrmann & Miller, 1978), the radius of gyration of the SUV at time t , R_{gt} , is given as


Figure 8

Change of SAXS curve of the SUVs of $[GD3]/[\text{cholesterol}]/[\text{PC}] = 0.1/0.1/1$ after jumping the KCl concentration from 0 mM to 50 mM. The SAXS curves at initial and final times are displayed.

$$R_{gt} = \left[R_0^2 + \frac{1}{\rho_t V} \int_V \rho_F(\mathbf{r}, t) r^2 d\mathbf{r} \right]^{1/2} \quad (9)$$

where R_0 is the mechanical radius of gyration which is independent on the contrast, $\rho_F(\mathbf{r}, t)$ is the scattering density fluctuation of the SUV against its average scattering density at an intermediate time t , which also depends on ρ_t . Therefore $\rho_F(\mathbf{r}, t)$ can be obtained by interpolating the $\rho_F(\mathbf{r}, t)$ at initial and final times, and equation (9) is then simplified as

$$R_{gt} = \left[\alpha R_{gi}^2 + (1 - \alpha) R_{gf}^2 \right]^{1/2} \quad (10)$$

where $\alpha = \exp(-P_D St/V_C)$, and R_{gi} and R_{gf} are the radii of gyration at initial and final times, respectively. The dotted lines in Fig. 7 show the least-squares fitting curves obtained using equation (10). The R_{gi} , R_{gf} and P for the SUV with the addition of 50 mM KCl are found to be 98.0 ± 0.5 Å, 124.9 ± 1.1 Å, and $(9.1 \pm 0.9) \times 10^{-4}$ cm s $^{-1}$, respectively. Here we gave the radius of the SUV to be ~ 185 Å from the $p(r)$ function in Fig. 6 and the bilayer width to be ~ 55 Å (Hirai *et al.*, 2003; Hayakawa & Hirai, 2003). In spite of the simple analysis the value obtained for the permeability of water across the membrane would be comparable with those values reported previously (Lande *et al.*, 1995). The present results indicate that the increase of K^+ ion concentration specifically enhances the permeability of water molecules through the lipid bilayer containing at appropriate amounts of G_{D3} and cholesterol as similar as in the intact raft membrane. Neuronal impulses or excitations caused by K^+ current would be ascribed to the presence of G_{D3} -cholesterol microdomains within the bilayers. The boundary between positive and negative hydrations is between the Na^+ and K^+ ions. K^+ ions increase the diffusion coefficient of water and reduce its viscosity; alternatively, water molecules around K^+ ions are more mobile (Maitov, 1981). In addition the sugar head portion of ganglioside is very hydrophilic and can occlude amounts of weakly bound water molecules that are easily released by changing temperature (Hirai *et al.*, 1996a,b, 1998b; Hayakawa & Hirai, 2002). Therefore, the present results indicate that K^+ ions would change the dynamics of the membrane to increase the permeability of water through the dehydration of G_{D3} -cholesterol rich clusters in the membrane.

The SANS, SAXS and WAXS experiments were done under the approval of the Neutron Scattering Program Advisory Committee (Proposal #03-189), of the Photon Factory Program Advisory Committee of KEK (Proposal #2004G177) and under the approval of the JASRI Program Advisory Committee (Proposal #2004A0399 & #2005-A0394).

References

- Hakomori, S. (2001). *Trends Glycosci. Glycotechnol.* **13**, 219–230.
- Hayakawa, T. & Hirai, M. (2002). *Eur. Biophys. J.* **31**, 62–72.
- Hayakawa, T. & Hirai, M. (2003). *J. Appl. Cryst.* **36**, 489–493.
- Heerklott, H. (2002). *Biophys. J.* **83**, 2693–2701.
- Hirai, M., Arai, S., Takizawa, T., Yabuki, S. & Nakata, Y. (1998a). *Thermochim. Acta*, **308**, 93–99.
- Hirai, M., Iwase, H. & Hayakawa, T. (1999). *J. Phys. Chem. B*, **103**, 10136–10142.
- Hirai, M., Iwase, H. & Hayakawa, T. (2001). *J. Phys. Soc. Jpn.* **70**, 420–423.
- Hirai, M., Iwase, H., Hayakawa, T., Koizumi, M. & Takahashi, H. (2003). *Biophys. J.* **85**, 1600–1610.
- Hirai, M., Iwase, H., Hayakawa, T., Miura, K. & Inoue, K. (2002). *J. Synchrotron Rad.* **9**, 202–205.

- Hirai, M., Koizumi, M., Hayakawa, T., Takahashi, H., Abe, S., Hirai, H., Miura, K. & Inoue, K. (2004). *Biochemistry*, **43**, 9036–9049.
- Hirai, M., Koizumi, M., Hirai, H., Hayakawa, T., Yuyama, K., Suzuki, N. & Kasahara, K. (2005). *J. Phys. Condens. Matter*, **17**, s2965-s2977.
- Hirai, M. & Takizawa, T. (1998b). *Biophys. J.* **74**, 3010–3014.
- Hirai, M., Takizawa, T., Yabuki, S. & Hayashi, K. (1996c). *J. Chem. Soc. Faraday Trans.* **92**, 4533–4540.
- Hirai, M., Takizawa, T., Yabuki, S., Hirai, T. & Hayashi, K. (1996b). *J. Phys. Chem.* **100**, 11675–11680.
- Hirai, M., Takizawa, T., Yabuki, S., Nakata, Y. & Hayashi, K. (1996a). *Biophys. J.* **70**, 1761–1768.
- Kasahara, K. & Sanai, Y. (2001). *Trends Glycosci. Glycotechnol.* **13**, 251–259.
- Kasahara, K., Watanabe, K., Takeuchi, K., Kaneko, H., Oohira, A., Kobayashi, S., Okumura, N., Okada, M. & Nagai, K. (1998). *J. Biochem. (Tokyo)*, **123**, 624–629.
- Kasahara, K., Watanabe, K., Takeuchi, K., Kaneko, H., Oohira, A., Yamamoto, T. & Sanai, Y. (2000). *J. Biol. Chem.* **275**, 34701–34709.
- Kasahara, K., Watanabe, Y., Yamamoto, T. & Sanai, Y. (1997). *J. Biol. Chem.* **272**, 29947–29953.
- Kawai, H., Allende, M. L., Wada, R., Kono, M., Sango, K., Deng, C., Miyakawa, T., Crawley, J. N., Werth, N., Bierfreund, U., Sandhoff, K. & Proia, R. I. (2001). *J. Biol. Chem.* **276**, 6885–6888.
- Lande, M. B., Donovan, J. M. & Ziedel, J. (1995). *J. Gen. Physiol.* **106**, 67–84.
- Ledeer, R. W., Hakomori, S., Yates, A. J., Schneider, J. S. & Yu, R. K. (1998). *Sphingolipids as Signaling Modulators in the Nervous System*. New York: The New York Academy of Sciences.
- Maitov, R. K. (1981). *DAN*, **260**, 1402–1408.
- Miura, K., Kawamoto, M., Inoue, K., Yamamoto, M., Kumasaka, T., Sugiura, M., Yamano, A. & Moriyama, H. (2000). *SPring-8 User Exp. Rep.* **4**, 168.
- Simons, K. & Ikonen, E. (1997). *Nature (London)*, **387**, 569–572.
- Simons, M., Keller, P., Strooper, B. D., Beyreuther, K., Dotti, C. G. & Simons, K. (1998). *Proc. Natl. Acad. Sci. USA*, **95**, 6460–6464.
- Simons, K. & Toomre, D. (2000). *Nat. Rev. Mol. Cell Biol.* **1**, 31–39.
- Stuhrmann, H. B. & Miller, A. (1978). *J. Appl. Cryst.* **11**, 325–345.
- Ueki, T., Hiragi, Y., Kataoka, M., Inoko, Y., Amemiya, Y., Izumi, Y., Tagawa, H. & Muroga, Y. (1985). *Biophys. Chem.* **23**, 115–124.
- Yamamoto, T. & Sanai, Y. (2000). *J. Biol. Chem.* **275**, 34701–34709.
- Yuyama, K., S-Suzuki, N., Sanai, Y. & Kasahara, K. (2003). *Trends Glycosci. Glycotechnol.* **15**, 139–151.